

Swept wing boundary-layer receptivity to localized surface roughness

David Tempelmann¹†, Lars-Uve Schrader¹, Ardeshir Hanifi^{1,2}, Luca Brandt¹
and Dan S. Henningson¹

¹ Linné Flow Centre, SeRC, KTH Mechanics, Stockholm, SE-100 44, Sweden

² Swedish Defence Research Agency, FOI, Stockholm, SE-164 90, Sweden

(Received 26 September 2011; revised 2 May 2012; accepted 8 August 2012;
first published online 20 September 2012)

The receptivity to localized surface roughness of a swept-wing boundary layer is studied by direct numerical simulation (DNS) and computations using the parabolized stability equations (PSEs). The DNS is laid out to reproduce wind tunnel experiments performed by Saric and coworkers, where micron-sized cylinders were used to trigger steady crossflow modes. The amplitudes of the roughness-induced fundamental crossflow wave and its superharmonics obtained from nonlinear PSE solutions agree excellently with the DNS results. A receptivity model using the direct and adjoint PSEs is shown to provide reliable predictions of the receptivity to roughness cylinders of different heights and chordwise locations. Being robust and computationally efficient, the model is well suited as a predictive tool of receptivity in flows of practical interest. The crossflow mode amplitudes obtained based on both DNS and PSE methods are 40 % of those measured in the experiments. Additional comparisons between experimental and PSE data for various disturbance wavelengths reveal that the measured disturbance amplitudes are consistently larger than those predicted by the PSE-based receptivity model by a nearly constant factor. Supplementary DNS and PSE computations suggest that possible natural leading-edge roughness and free-stream turbulence in the experiments are unlikely to account for this discrepancy. It is more likely that experimental uncertainties in the streamwise location of the roughness array and cylinder height are responsible for the additional receptivity observed in the experiments.

Key words: boundary layer receptivity, boundary layer stability

1. Introduction

Receptivity models describe how an external disturbance environment is filtered by the boundary layer. Free-stream turbulence, acoustic noise or surface roughness represent the most common external disturbances. The receptivity process is often neglected in transition prediction models. However, it has been shown in experiments by Saric and coworkers and by Bippes and coworkers (an overview can be found in Saric, Carillo & Reibert (1998*b*), Bippes (1999) and Saric, Reed & White (2003)) that the transition scenario in three-dimensional boundary layers strongly depends on the external disturbance environment. In environments exhibiting high

† Present address: KTH Mechanics. Email address for correspondence: david@mech.kth.se

levels of free-stream turbulence, unsteady boundary-layer disturbances dominate over stationary disturbances excited by surface roughness. Conversely, in low-level turbulence environments, such as free flight, stationary disturbances dominate. Similar results were obtained by Schrader, Brandt & Henningson (2009) and Schrader, Amin & Brandt (2010), who performed DNS of different receptivity mechanisms as well as large-eddy simulations of a swept-flat-plate boundary layer subject to different levels of free-stream turbulence and to surface roughness. Hence, robust transition models should account for receptivity.

The receptivity of crossflow disturbances to surface irregularities in three-dimensional boundary layers was initially studied at finite Reynolds numbers by Fedorov (1988), Manuilovich (1989), Crouch (1993) and Choudhari (1994). One conclusion of the two latter studies was that steady crossflow disturbances are likely to dominate over their unsteady counterparts for characteristic acoustic noise levels apparent in free flight. However, it has been found by Collis & Lele (1999), for example, that the assumption of locally parallel flow leads to an over-prediction of receptivity amplitudes. Collis & Lele (1999) studied the receptivity to surface roughness near a swept leading edge using DNS and compared results with finite Reynolds number theory (FRNT). They found non-parallel effects to be dominant over curvature effects, leading to a reduction in receptivity amplitudes as compared to FRNT predictions. Similarly, Bertolotti (2000) found that non-parallel effects decreased receptivity amplitudes in three-dimensional boundary layers subject to localized wall roughness. He used a non-parallel Fourier transform methodology as well as direct solutions of the linearized Navier–Stokes equations (LNSEs). Further, he obtained good agreement with the DLR Prinzip experiments by Deyhle & Bippes (1996) and Bippes (1999). Another notable investigation of receptivity of crossflow instabilities to roughness elements on a swept cylinder was performed by Piot, Content & Casalis (2008) using DNS.

An efficient approach to including non-parallel effects in receptivity prediction is to use the adjoint of the PSEs, as done by Hill (1997) and Chang & Choudhari (2005) for both two- and three-dimensional boundary layers and Airiau (2000) and Airiau, Walther & Bottaro (2002) for two-dimensional boundary layers. Dobrinsky (2002) employed direct and adjoint PSEs to predict receptivity of three-dimensional boundary layers and obtained good agreement with solutions of the LNSEs.

Recently, substantial effort has been put into modelling the swept-wing in-flight testing (SWIFT) experiments performed at Texas A&M University Flight Research Laboratory (Carpenter, Saric & Reed 2009). Both DNS and PSE methods have been employed to model the excitation of crossflow disturbances by distributed roughness elements in the SWIFT boundary layer (Rizzetta *et al.* 2010; Carpenter *et al.* 2010). However, so far, no detailed comparisons between disturbance amplitudes predicted numerically and those obtained from experiments have been made.

In this study we focus on the excitation of crossflow disturbances by localized surface roughness. The case considered is a swept-wing boundary layer, which has been studied experimentally by Saric and coworkers at Arizona State University ('ASU experiments': see e.g. Reibert 1996; Reibert *et al.* 1996; Saric, Carillo & Reibert 1998*a*). Several attempts have been made to model these experiments, both numerically and theoretically. Ng & Crouch (1999) modelled the receptivity using FRNT, which is based on the parallel flow assumption, and obtained receptivity amplitudes close to the experimental ones. Haynes & Reed (2000) were able to correctly predict the nonlinear disturbance evolution by solving the nonlinear parabolized stability equations (NPSEs). However, instead of incorporating the

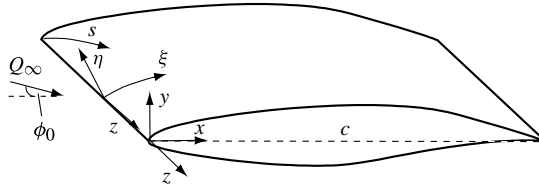


FIGURE 1. Swept NLF(2)-0415 wing, with sweep angle ϕ_0 and the total incoming velocity Q_∞ : (ξ, η, ζ) and (x, y, z) represent curvilinear and Cartesian coordinate systems respectively, while s denotes the direction parallel to the incoming free stream which is tangential to the wing surface. Note that the wing is at an angle of attack of -4° (not shown in the figure).

receptivity phase in their numerical model, Haynes & Reed (2000) extracted the initial amplitudes from experimental data. T. Nishino and K. Shariff (personal communication) performed a DNS but obtained receptivity amplitudes far below those measured in the experiments, suspecting their roughness model may be inadequate.

The aim of this study is to carefully compare different approaches to modelling boundary-layer receptivity to surface roughness. We use both DNS and PSE methods. The latter may be combined with solutions to the respective adjoint equations to predict receptivity. Finally, we compare our work with the FRNT results by Ng & Crouch (1999) in order to assess the implications of the parallel flow approximation on the quality of the receptivity prediction.

2. Flow configuration

We examine the flow over a swept wing (NLF(2)-0415 aerofoil, Somers & Horstmann 1985) mounted in a wind tunnel. This flow configuration was studied experimentally by Reibert (1996) and Reibert *et al.* (1996). In order to obtain a strong negative pressure gradient on the upper wing side, and thus a strong crossflow instability, a sweep angle of $\phi_0 = 45^\circ$ and an angle of attack of $\alpha_a = -4^\circ$ are chosen. The latter is defined in a plane normal to the leading edge. The location of the rotation axis is at 25 % chord from the leading edge. The distance of the axis is 0.6 m from the upper wind tunnel wall. Three chord Reynolds numbers, $Re_C = Q_\infty C/\nu = 1.6 \times 10^6$, 2.4×10^6 and 3.2×10^6 , are studied. Here, C denotes the long, swept chord which is related to the unswept chord c through $C = c\sqrt{2}$, Q_∞ represents the total incoming free-stream velocity, and ν is the kinematic viscosity.

In the experiments, crossflow disturbances were excited in a controlled manner by placing a spanwise array of micron-sized roughness elements with spacing L_r at $x/c = 0.023$, where x denotes the chordwise direction (see figure 1). Reibert *et al.* (1996) used circular roughness cylinders with height $\varepsilon_r = 6 \mu\text{m}$ and diameter $d_r = 3.7 \text{ mm}$. In the present study, the experimental cases are modelled using DNS and PSE methods. Additional direct numerical simulations for cases not considered by Reibert (1996) are presented (e.g. different roughness heights, different roughness positions). These provide insight into different parameter effects and help to cross-validate both the DNS and PSE methods. Table 1 provides an overview of the cases studied in this paper and the respective methods employed. Owing to the cost of direct numerical simulations, not all cases have been studied by DNS.

2.1. Coordinate systems and velocity profiles

The aerofoil and the adopted coordinate systems are shown in figure 1. Here, (x, y, z) denote the chordwise, normal-to-the-chord and spanwise directions. Further, we use

Reynolds number Re_c	Spacing L_r (mm)	Roughness location x_r/c	Height ε_r (μm)	Diameter d_r (mm)	Methods
2.4×10^6	12	0.023	6 μm	3.7	exp./DNS/PSE/FRNT
2.4×10^6	12	0.025	6	3.7	DNS/PSE
2.4×10^6	12	0.027	6	3.7	DNS/PSE
2.4×10^6	12	0.044	6	3.7	DNS/PSE
2.4×10^6	12	0.086	6	3.7	DNS/PSE
2.4×10^6	12	0.129	6	3.7	DNS/PSE
2.4×10^6	12	0.025	12	3.7	DNS
2.4×10^6	12	0.025	60	3.7	DNS
2.4×10^6	12	0.025	120	3.7	DNS
1.6×10^6	12	0.023	6	3.7	exp./PSE/FRNT
3.2×10^6	12	0.023	6	3.7	exp./PSE/FRNT
2.4×10^6	36	0.023	6	3.7	exp./PSE/FRNT

TABLE 1. Overview of flow cases studied in this paper together with the respective methods employed (experiment, DNS, PSE, FRNT). The abbreviation ‘exp.’ refers to the experiments by Reibert (1996) and Reibert *et al.* (1996), while ‘FRNT’ stands for finite Reynolds number theory and denotes the results by Ng & Crouch (1999).

a reference coordinate system $(\underline{x}, \underline{y}, \underline{z})$ which coincides with (x, y, z) at $\alpha_a = 0^\circ$, and (U, V, W) represent the respective velocity components. The body-fitted curvilinear coordinates (ξ, η, z) define the tangential, wall-normal and spanwise directions. The corresponding velocity components are denoted by (U_ξ, V_η, W) . The experimental measurements by Reibert *et al.* (1996) were evaluated using a coordinate system aligned with the incoming free stream, i.e. the s -direction in figure 1. When comparing with experimental results we follow Ng & Crouch (1999) and use the velocity component $U_{s,n}$, which is obtained according to

$$U_{s,n} = U_\xi \cos \phi_0 + W \sin \phi_0. \quad (2.1)$$

Note that the experimental velocity profiles $U_{s,e}$ measured by Reibert *et al.* (1996) slightly deviate from the definition presented above, for the following reasons. First, the experimental coordinate system was not curvilinear, i.e. the hot-wire probe was not traversed in the η - but in the y -direction. Secondly, $U_{s,e}$ represents the total velocity parallel to the s -plane, i.e. it includes the wall-normal velocity component whereas $U_{s,n}$ represents the wall-tangential component only. However, Ng & Crouch (1999) point out that a comparison between $U_{s,n}$ and $U_{s,e}$ is adequate, because the experimental measurements were taken at positions downstream of $x/c = 0.1$ where the wing surface curvature is weak and wall-normal velocity components are negligibly small. This is justified in appendix A by a comparison where the disturbance amplitudes are evaluated according to the present definition and that by Reibert *et al.* (1996). The amplitudes match favourably with no visible difference. For this reason, we will drop the subscripts n and e and simply write U_s in the remainder of the text.

3. Methodology

3.1. Direct numerical simulations

The spectral element method (SEM) has been used to perform the direct numerical simulations of the swept-wing flow. The SEM, introduced by Patera (1984), provides

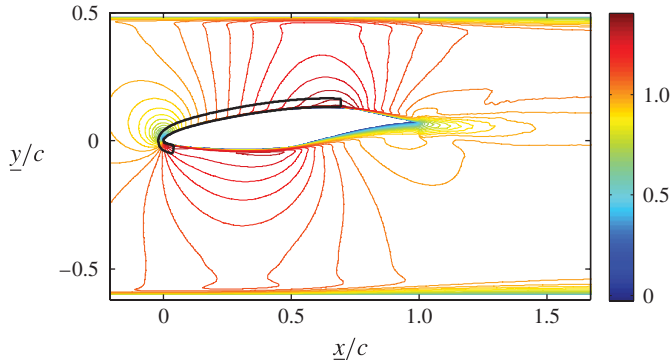


FIGURE 2. Excerpt of the velocity field (U-component) obtained from a RANS solution of the entire wind tunnel test section. The black solid line denotes the baseflow domain.

spectral accuracy in space while allowing for the geometrical flexibility of finite element methods. We use the ‘Nek5000’ simulation code developed by Fischer, Lottes & Kerkemeier (2008) which allows us to solve both the nonlinear and linearized Navier Stokes equations. The code is very accurate for both laminar and turbulent flows; see e.g. Ohlsson *et al.* (2011) for a validation for turbulent channel flow. The spatial discretization is obtained by decomposing the physical domain into spectral elements, which in turn are subdivided into arrays of Gauss–Lobatto–Legendre (GLL) nodes for the velocity and Gauss–Legendre (GL) nodes for the pressure field. The solution to the Navier–Stokes equations is approximated element-wise as a sum of Lagrange interpolants defined by an orthogonal basis of Legendre polynomials up to degree N . The following results have been obtained using $N = 11$ for the velocity grids and $N = 9$ for the pressure grids. The staggered pressure grid makes the specification of pressure boundary conditions unnecessary. This choice is referred to as a $\mathbb{P}_N - \mathbb{P}_{N-2}$ discretization (Maday & Patera 1989). The present SEM code is optimized for MPI-based usage on supercomputers with thousands of processors (Tufo & Fischer 2001). Here, we have performed parallel computations on up to 2048 processors. Three types of DNS have been carried out. First, a steady baseflow has been computed which serves to provide initial and boundary conditions for a second nonlinear DNS of the perturbed flow. Further, the steady baseflow has been used for simulations of the LNSEs, which help to assess the performance of linear roughness models based on inhomogeneous boundary conditions (see § 3.1.2).

3.1.1. Baseflow

A preliminary Reynolds-averaged Navier–Stokes (RANS) simulation of the flow in the entire wind tunnel test section is carried out in order to explore the flow field and select a suitable domain for the main DNS. The RANS is solved using the EDGE code developed at FOI (Eliasson 2002). The solution is three-dimensional, but the flow is assumed to be homogeneous in the spanwise direction. The resulting flow field is presented in figure 2, where the numerical domain of the main simulation is also shown. A steady, spanwise invariant baseflow is computed by DNS on this domain, using no-slip, zero-stress and periodic boundary conditions at the wall, the outflow and the lateral boundaries, respectively. At the free-stream boundary, all three velocity components extracted from the RANS solution are prescribed as Dirichlet conditions. Since the baseflow is homogeneous in the spanwise direction, the spanwise momentum equation is decoupled from the other two momentum equations and acts as a passive

scalar transport. The three-dimensional baseflow velocity field can thus be obtained at a significantly lower computational cost by solving a two-dimensional problem and one passive scalar equation instead of the full three-dimensional problem. The domain size chosen extends from $x/c = 0.04$ on the lower wing side to $x/c = 0.7$ on the upper wing side. Although we are only interested in the flow field on the upper wing side, we have retained parts of the flow on the lower side to account for the asymmetry of the configuration. It should be noted that the laminar flow separates from the lower wing side slightly downstream of the leading edge ($\sim 0.5\%c$). This separation was also observed by T. Nishino and K. Shariff (personal communication). When solving the RANS, the separation is eliminated by assuming a turbulent flow downstream of the separation location, where a $k - \omega$ turbulence model (Hellsten 2005) based on the explicit version of the algebraic Reynolds stress model (EARSIM) by Wallin & Johansson (2000) has been used. A sponge region is inserted in the DNS in order to obtain a steady baseflow without a local, numerically destabilizing backflow at the lower outlet. Within this sponge region, the flow is forced towards the time average of the separation bubble. This is accomplished by adding the forcing term

$$\mathbf{F}(\mathbf{x}, t) = A_{max}\lambda_f(\mathbf{x})[\mathbf{U}_f(\mathbf{x}) - \mathbf{U}(\mathbf{x}, t)] \quad (3.1)$$

on the right-hand side of the momentum equations. The field $\mathbf{U} = (U, V, W)^T$ stands for the instantaneous separated flow field and \mathbf{U}_f denotes the enforced flow (containing the time averaged separation bubble). The quantity λ_f takes the form of a smooth step function (see Schrader *et al.* 2009) and varies between zero and one in the separated region while vanishing everywhere else. The coefficient A_{max} determines the maximal strength of the forcing and is $A_{max} = 2.5$ here. This choice ensures a fast convergence to a steady state while still rendering the simulation numerically stable. Since the sponge forcing is proportional to the difference between the ‘target’ and the actual flow, \mathbf{F} is significant only in the separated boundary layer while decaying to zero in the free stream.

The computational mesh used for the DNS of the baseflow is presented in figure 3(a). It has been generated using the *gridgen-c* code by Sakov (2011), which represents an implementation of the Schwarz–Christoffel transformation and provides quasi-orthogonal grids. The mesh consists of 3267 two-dimensional spectral elements.

3.1.2. Perturbed flow

In order to excite steady crossflow modes, a single roughness element of the form of a shallow cylindrical disk is inserted near the leading edge of the swept wing. The roughness is designed to match one of the circular cylinders of the spanwise roughness array used in the ASU experiments (Reibert *et al.* 1996). We mimic the roughness row by prescribing spanwise periodic boundary conditions. By comparing with simulations involving two roughness elements, this treatment was shown in Schrader *et al.* (2011) to be adequate for modelling a spanwise cyclic roughness array. The parameters of the roughness disks are listed in table 1. The computational mesh used for the DNS of the perturbed flow as well as the intra-elemental GLL mesh for a polynomial order $N = 11$ are shown in figure 3. The inflow is located at $x/c = 0.088$ on the upper wing side at a distance of $4.6d_r$ upstream of the rising flank of the roughness cylinder. Downstream of this location, the mesh is identical to that used to obtain the baseflow; however, since the perturbed flow varies in the spanwise direction, the two-dimensional mesh presented in figure 3 is extended in the z direction. Ten spectral elements are used to resolve a span of length L_r (see table 1). This choice ensures a sufficiently fine discrete representation of the circular roughness disk. The total number of three-dimensional elements amounts to 29 150. The Dirichlet boundary

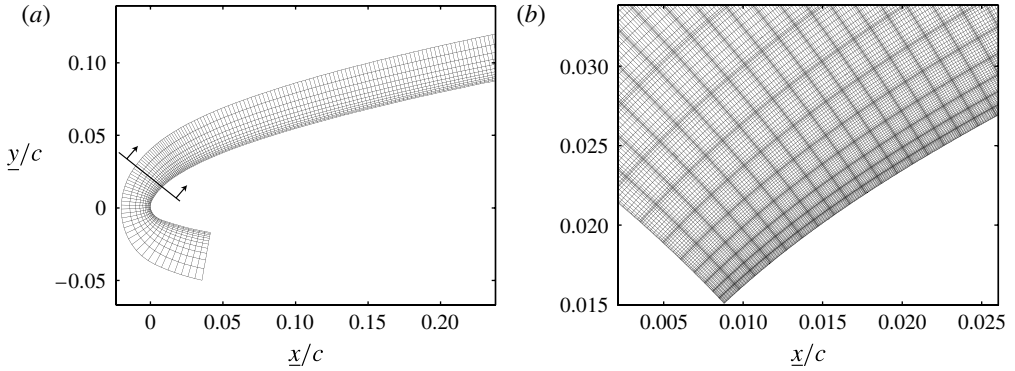


FIGURE 3. (a) Computational mesh used for direct numerical simulations of both the baseflow and the perturbed flow. Only the spectral elements are shown. For the baseflow simulations the complete domain shown was considered. For simulations of the perturbed flow only the domain to the right of the black solid line, denoted by the two arrows, was used. Hence, the lower wing part and the leading-edge region were not accounted for. (b) A close-up of the initial region of the computational mesh used for the perturbed flow showing the intra-elemental GLL mesh.

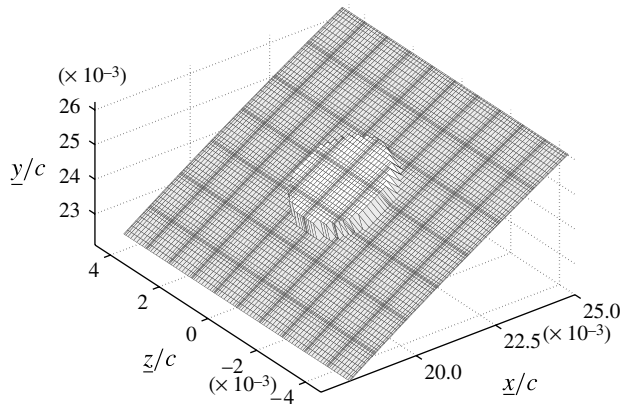


FIGURE 4. Meshed cylindrical roughness element generated by displacing the GLL points. For visualization purposes the height is scaled by a factor of 100.

conditions required at the inflow plane have been extracted from the DNS solution of the baseflow.

Two different approaches have been considered to predict the receptivity of the swept-wing boundary layer to the surface roughness. The first approach consists in meshing the circular roughness disk in order to obtain a realistic representation of the roughness element (see figure 4). The resolution in the streamwise direction is maximum at the roughness location and chosen such that 2.5 spectral elements resolve the roughness disk in the ξ - and ζ -directions. The spectral elements at the roughness site are much higher (~ 120 times) than the roughness cylinder, which is hardly visible in figure 3(b) despite the enlargement. Therefore, the roughness can be modelled by a displacement of the corresponding GLL points at the wall. The GLL points in the

interior of the affected elements have been adjusted so as to ensure a correct GLL distribution in the wall-normal direction.

The second approach is appropriate for many DNS methods, where it is difficult – if not impossible – to incorporate in the computational mesh roughness elements with heights of the order of 1% of the boundary-layer thickness. Also, many simplified methods, e.g. the parabolized stability equations (see § 3.2), are incapable of handling meshed roughness elements. In such cases, a different approach is commonly used which builds on the representation of the roughness elements by inhomogeneous boundary conditions along the wall. The spectral element method enables us to consider both approaches (the meshed and the modelled roughness) and to compare their performance. The roughness model is implemented by projecting the no-slip boundary conditions at the roughness to the smooth, undisturbed wall. The projection is performed in the wall-normal direction using Taylor series expansions. The wall boundary conditions thus become

$$u_{i,w} = -(x_r - x_w) \frac{\partial U_i}{\partial x} \Big|_{x_w, y_w} - (y_r - y_w) \frac{\partial U_i}{\partial y} \Big|_{x_w, y_w} + \dots, \quad (3.2)$$

where lowercase and uppercase letters denote disturbance and baseflow quantities, respectively. The subscript i represents velocity components (u, v, w), and the subscripts r and w label the coordinates of the rough and the undisturbed wall, respectively. When using the roughness model we solve the LNSEs instead of the full nonlinear equations.

3.2. Parabolized stability equations

The parabolized stability equations (PSEs), which were independently proposed by Herbert & Bertolotti and Dallmann & Simen (see e.g. Chang *et al.* 1991; Simen 1992; Herbert 1997), have been widely used to predict the linear and nonlinear evolution of disturbances in convectively unstable flows. Here, we give a brief introduction to the linear PSEs as these will be used to predict receptivity to surface roughness. Details of the derivation of the linear PSEs can be found in Hanifi *et al.* (1994). A thorough description of the nonlinear extension (NPSE) is given by Bertolotti, Herbert & Spalart (1992) and Herbert (1997). Here, the ‘NOLOT’ code (see Hein, Hanifi & Casalis 2000) has been used for solving the NPSEs.

3.2.1. Introduction to PSEs

The linear PSEs build on assuming disturbances of the form

$$\mathbf{q}'(\xi, \eta, z, t) = \mathbf{q}(\xi, \eta) \Theta(\xi) \exp i(\beta z - \omega t) \quad (3.3a)$$

$$\Theta(\xi) = \exp \left(i \int_{\xi_0}^{\xi} \alpha(\xi') d\xi' \right), \quad (3.3b)$$

where $\mathbf{q} = (u_\xi, v_\eta, w, p)^T$, and (ξ, η, z) establish orthogonal curvilinear coordinates (see figure 1). The corresponding tangential and spanwise wavenumbers are (α, β) , while the angular frequency and time are denoted by ω and t . Note that α is chosen to be a complex number. For clarity, we introduce

$$\hat{\mathbf{q}}(\xi, \eta) = \mathbf{q}(\xi, \eta) \Theta(\xi). \quad (3.4)$$

After introducing ansatz (3.3) into the LNSEs and assuming a scale separation between the weak variation in the ξ -direction and the strong variation in the η -direction (see Hanifi *et al.* 1994 for details), various terms including the second derivatives with

respect to ξ can be neglected, which yields a nearly parabolic system of equations of the form

$$\mathbf{A}\mathbf{q} + \mathbf{B}\frac{\partial\mathbf{q}}{\partial\eta} + \mathbf{C}\frac{\partial^2\mathbf{q}}{\partial\eta^2} + \mathbf{D}\frac{1}{h_1}\frac{\partial\mathbf{q}}{\partial\xi} = 0, \quad (3.5)$$

where \mathbf{A} , \mathbf{B} , \mathbf{C} and \mathbf{D} are linear operators (see appendix B). The scaling factor that arises due to the orthogonal curvilinear metric is given by $h_1^2 = \sum_{j=1}^3 (\partial x_j / \partial \xi)^2$, where x_i represents the Cartesian coordinates of the reference system. It should be noted that we neglect the disturbance pressure gradient term $\partial p / \partial \xi$, since it introduces some residual ellipticity rendering the solution scheme unstable for step sizes below a certain threshold (see Haj-Hariri 1994; Andersson, Henningson & Hanifi 1998). This is motivated by the studies of Tempelmann, Hanifi & Henningson (2010, 2012), who have shown that this term is negligible for crossflow-dominated boundary layers.

Since both \mathbf{q} and α in ansatz (3.3) are functions of ξ , an auxiliary condition of the form

$$\int_0^\infty \mathbf{q}^H \frac{\partial\mathbf{q}}{\partial\xi} d\eta = 0 \quad (3.6)$$

is introduced, ensuring that both the growth and the periodic variations of the disturbance are absorbed by the exponential part of (3.3). The PSEs are solved by marching in the downstream direction, starting with a solution to the local stability problem. The coupled nonlinear system of (3.5) and (3.6) is solved iteratively at each position while for the homogeneous PSEs the Dirichlet boundary conditions $(u_\xi, v_\eta, w) = 0$ are imposed in the free stream and at the smooth wall.

3.2.2. Receptivity

The use of adjoint solutions to predict the receptivity of boundary layers was introduced by Fedorov (1988) and Hill (1995, 1997). Hill noted that ‘adjoint eigensolutions act as a filter on a general disturbance field, enabling us to identify the amplitude of the corresponding eigenmode’. Similarly, the adjoint PSEs derived in the following will enable us to determine the receptivity amplitudes of disturbances excited by surface roughness. The adjoint PSEs are defined by constructing a Lagrange identity of the form

$$\langle \mathbf{q}^*, \mathcal{L}\mathbf{q} \rangle = \langle \mathcal{L}^*\mathbf{q}^*, \mathbf{q} \rangle + \iint_\Omega \nabla \cdot \mathcal{J}(\mathbf{q}, \mathbf{q}^*) h_1 d\xi d\eta, \quad (3.7)$$

where \mathcal{L} is a linear operator and $\mathcal{L}\mathbf{q}$ is a compact notation of (3.5), \mathcal{J} is the bilinear concomitant, comprising terms at the boundary of domain Ω , and ‘*’ denotes adjoint quantities. The adjoint state vector is defined by $\mathbf{q}^* = (p^*, u_\xi^*, v_\eta^*, w^*)^T$. The inner product is defined according to

$$\langle \mathbf{a}, \mathbf{b} \rangle = \iint_\Omega \mathbf{a}^H \mathbf{b} h_1 d\xi d\eta \quad (3.8)$$

for some \mathbb{C}^n -valued functions \mathbf{a} and \mathbf{b} , and $\Omega = [\xi_0, \xi_1] \times [0, \infty]$. The superscript H denotes a conjugate transpose. Here $\mathcal{L}^*\mathbf{q}^* = 0$ stands for the adjoint PSEs, obtained by employing integration by parts on the leftmost inner product of (3.7). A detailed derivation of (3.7) is given in appendix C. By imposing the Dirichlet boundary conditions $(u_\xi^*, v_\eta^*, w^*) = 0$ in the free stream and at the wall as well as $(u_\xi, v_\eta, w) = 0$

in the free stream, (3.7) becomes

$$\int_0^{\infty} [(\mathbf{q}^*)^H \mathbf{D}\mathbf{q}]_{\xi_0}^{\xi_1} d\eta = \int_{\xi_0}^{\xi_1} \left[(\mathbf{q}^*)^H \mathbf{B}\mathbf{q}h_1 - \left(\frac{\partial \mathbf{q}^*}{\partial \eta} \right)^H \mathbf{C}\mathbf{q}h_1 \right]_{\eta=0} d\xi, \quad (3.9)$$

provided that \mathbf{q} and \mathbf{q}^* are solutions to the PSEs and adjoint PSEs, respectively. Next, we introduce

$$J(\xi) = \int_0^{\infty} (\mathbf{q}^*)^H \mathbf{D}\tilde{\mathbf{q}} d\eta, \quad (3.10)$$

where $\tilde{\mathbf{q}} = \hat{\mathbf{q}}/A$ has been normalized by a complex-valued amplitude $A(x) = \hat{u}_s(x, \eta_{max})$. Here, η_{max} denotes the wall-normal position at which $|\hat{u}_s|$ takes its maximum value. It follows that

$$\Theta^{-1}AJ = \int_0^{\infty} (\mathbf{q}^*)^H \mathbf{D}\mathbf{q} d\eta. \quad (3.11)$$

Replacing the integral term on the left-hand side of (3.9) with expression (3.11) and introducing $\mathbf{q} = \Theta^{-1}\hat{\mathbf{q}}$ leads to

$$A(\xi_1) = \frac{\Theta}{J} \bigg|_{\xi_1} \left([\Theta^{-1}AJ]_{\xi_0} + \int_{\xi_0}^{\xi_1} \Theta^{-1} \left[(\mathbf{q}^*)^H \mathbf{B}\hat{\mathbf{q}}h_1 - \left(\frac{\partial \mathbf{q}^*}{\partial \eta} \right)^H \mathbf{C}\hat{\mathbf{q}}h_1 \right]_{\eta=0} d\xi \right). \quad (3.12)$$

Expression (3.12) yields the receptivity amplitude of disturbances excited by arbitrary inhomogeneous boundary conditions at the wall provided that these boundary conditions do not affect the shape but only the amplitude and the phase of the perturbation \mathbf{q}' . This assumption implies that $J(\xi)$ can be evaluated based on the solution of the homogeneous PSEs. Note that in the homogeneous case the left-hand side of (3.9) is conserved, i.e. $\Theta^{-1}AJ$ is conserved.

The receptivity of boundary-layer disturbances to surface roughness can now be obtained by assuming a zero-amplitude incoming disturbance, i.e. $A(\xi_0) = 0$, and by modelling the surface roughness by inhomogeneous boundary conditions (see (3.2)). For a body-fixed curvilinear coordinate system, the corresponding disturbance velocities at the wall become

$$\hat{u}_{\xi,w}(\xi) = - \frac{\partial U_{\xi}}{\partial \eta} \bigg|_{\eta=0} H_{\beta}(\xi), \quad (3.13a)$$

$$\hat{v}_{\eta,w}(\xi) = 0, \quad (3.13b)$$

$$\hat{w}_w(\xi) = - \frac{\partial W}{\partial \eta} \bigg|_{\eta=0} H_{\beta}(\xi). \quad (3.13c)$$

The cylindrical roughness element is represented by discrete Fourier modes $H_{\beta}(\xi)$ in the spanwise direction. If (3.13) is inserted into (3.12), we obtain the receptivity amplitude as

$$A(\xi_1) = \frac{-1}{J(\xi_1)Re} \int_{\xi_0}^{\xi_1} \exp \left(i \int_{\xi}^{\xi_1} \alpha(\xi') d\xi' \right) H_{\beta}(\xi) \left[\frac{\partial \bar{u}_{\xi}^*}{\partial \eta} \frac{\partial U_{\xi}}{\partial \eta} h_1 + \frac{\partial \bar{w}^*}{\partial \eta} \frac{\partial W}{\partial \eta} h_1 \right]_{\eta=0} d\xi, \quad (3.14)$$

with (ξ_0, ξ_1) being some arbitrary positions upstream and downstream of the roughness element, respectively. An overbar denotes complex conjugates. J is evaluated for the

undisturbed, homogeneous case. Equation (3.14) shows that the receptivity is evaluated from the adjoint variables and the baseflow shear at the wall. This procedure permits the extraction of the receptivity amplitude pertaining to a certain crossflow mode for any roughness shape and position from one single solution of the direct and adjoint PSEs. In the following we present receptivity amplitudes as

$$A_s = \frac{|A|}{\sqrt{2}} = \max_{\eta} \frac{|\hat{u}_s|}{\sqrt{2}}. \quad (3.15)$$

The factor $\sqrt{2}$ is used to obtain a root-mean-square (r.m.s.) amplitude with respect to the spanwise direction. For a detailed discussion on experimental and numerical disturbance amplitudes the reader is referred to appendix A.

3.2.3. Numerical scheme

The PSEs (3.5) are solved in MATLAB. The equation system is discretized using Chebyshev polynomials in the wall-normal direction. We use the ‘MATLAB differentiation matrix suite’ by Weideman & Reddy (2000). The Gauss–Lobatto collocation points are mapped to the domain $[0, \eta_{max}]$ and clustered near the wall; see Hanifi, Schmid & Henningson (1996) for details of the mapping technique. A second-order backward finite-difference scheme is employed to discretize the tangential direction ξ . The adjoint PSEs are discretized accordingly and marched from ξ_1 to ξ_0 . Note that the adjoint PSEs do not require an auxiliary condition of the type (3.6) since α has already been determined through the solution of the direct problem. Both the direct and the adjoint PSEs are initialized at ξ_0 and ξ_1 , respectively, with solution being the corresponding direct and adjoint local stability problem.

The baseflow contained in the linear operators of (3.5) is obtained by solving the quasi-three-dimensional, fully non-similar boundary-layer equations (BLEs: see Schlichting 1979), where the flow conditions required at the boundary-layer edge are retrieved from the pressure coefficient of the DNS solution. Although we could also use the computationally costly DNS baseflow in (3.5), our purpose here is to design an efficient transition prediction tool by combining the PSE method with a fast BLE solver. We will show in §§ 4 and 5.1 that using the approximate BLE solution instead of the full DNS baseflow produces satisfactory results. The BLEs are solved by employing second-order finite differences in both the ξ - and the η -directions starting from the stagnation point and neglecting curvature effects.

4. Baseflow results

The baseflow of the DNS is validated by a comparison with experimental results and solutions to the BLEs. The pressure coefficients extracted from the RANS and DNS solutions are compared to experimental measurements by Reibert *et al.* (1996) and to inviscid results by Haynes & Reed (2000), who employed a panel method (see figure 5). The pressure coefficient calculated from the RANS flow field is in excellent agreement with the experimental results. While the pressure coefficient obtained from DNS and that by Haynes & Reed (2000) agree well with each other, they lie slightly below the experimental results. This deviation seems to originate from the different modelling of the separation region on the lower wing side. When solving the RANS, this region has been assumed to be turbulent, which – based on the present c_p -comparison – appears to be a reasonable assumption. The absence of turbulent flow in the DNS and the inviscid approach by Haynes & Reed (2000) leads to a slight displacement of the stagnation point as compared to the RANS solution,

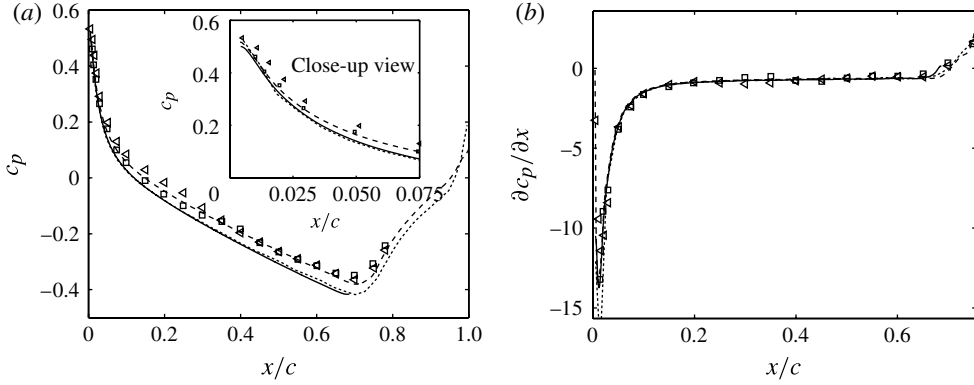


FIGURE 5. (a) Pressure coefficients c_p and (b) respective pressure gradients obtained from DNS (—), RANS (---), Haynes & Reed (2000) (···), and experiments with two different sensor locations (\triangleleft and \square).

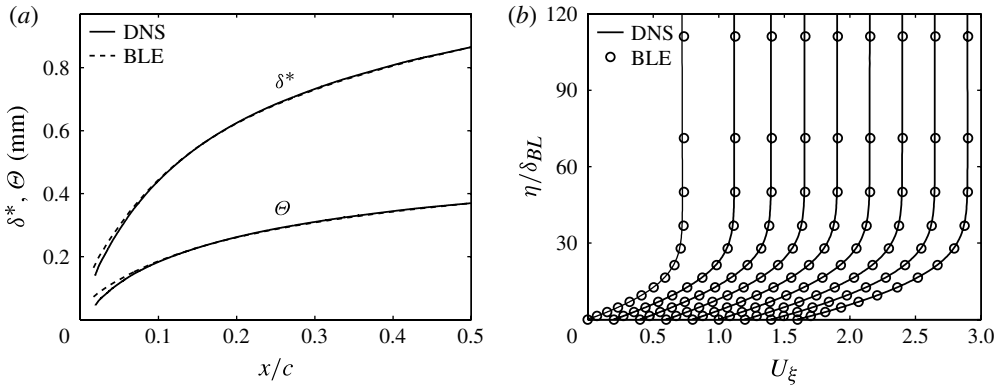


FIGURE 6. Comparison of (a) displacement and momentum loss thickness and (b) profiles U_ξ obtained from the DNS and the BLE solution for $Re_c = 2.4 \times 10^6$. Note that the profiles U_ξ are shifted according to $U_{\xi,k} = U_\xi + 0.2k$, where $k = 0, 2, \dots, 8$ changing from the leftmost to the rightmost profile in (b). The profiles are evaluated at $x/c = 0.03, 0.07, 0.12, 0.17, 0.23, 0.3, 0.37, 0.45, 0.55$. Note that η is normalized with the Blasius length scale $\delta_{BL} = \sqrt{\nu c / U_{\xi,edge}}$.

thus weakly affecting the pressure coefficient. However, several auxiliary computations using PSEs (see § 5.2) show that the influence of the small differences in c_p on the disturbance growth and the receptivity is negligible. This might be explained by the fact that the respective pressure gradients are very similar (see figure 5b). Haynes & Reed (2000) also found excellent agreement between the experimental measurements and the disturbance growth predicted by NPSEs when using the ‘inviscid’ pressure coefficient. In the following, we will therefore solve the BLEs based on the pressure coefficient obtained from DNS (see § 3.2.3) unless otherwise specified. The same pressure coefficient is used for different Reynolds numbers assuming viscous effects on c_p to be small.

Figure 6 compares the displacement thickness δ^* , the momentum loss thickness Θ and the boundary-layer profiles of U_ξ obtained from DNS and BLE calculations. Both

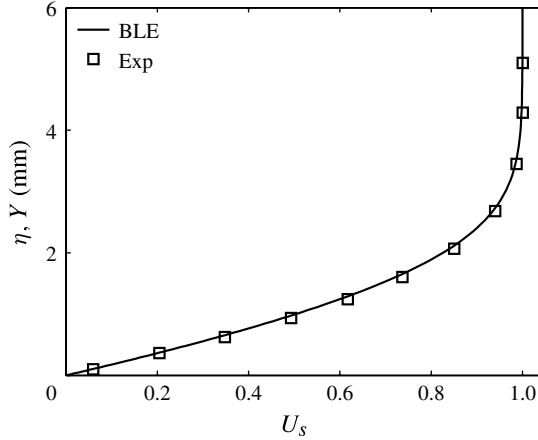


FIGURE 7. Comparison of boundary-layer profiles U_s at $x/c = 0.5$ obtained from the BLEs (plotted versus η) and experiments (plotted versus $Y = \underline{y} - \underline{y}_{wall}$) for $Re = 1.6 \times 10^6$.

δ^* and Θ are computed based on U_ξ . We obtain good agreement for all quantities, especially for positions farther downstream. The slight differences seen upstream may be explained by the assumption of slow variation in the ξ -direction, which is essential to the BLEs. However, this assumption is questionable close to the stagnation point, where the flow changes rapidly.

Because experimental measurements of the undisturbed flow profiles only exist for $Re_c = 1.6 \times 10^6$, while DNS data are solely available for $Re_c = 2.4 \times 10^6$ (see table 1), we compare the experimental boundary-layer profiles for U_s with our BLE results only, noticing favourable agreement at $x/c = 0.5$ (see figure 7). This shows that the wing surface curvature is weak and that the difference between η and $Y = \underline{y} - \underline{y}_{wall}$ is negligible. In conclusion, the present results confirm the validity of our numerical set ups for the DNS and the BLE computations. In the following, the DNS baseflow will be used for spectral element simulations of the LNSEs, while the BLE baseflow is employed to solve the PSEs.

5. Receptivity to surface roughness

Next, DNS and PSE results of the roughness-induced perturbation are presented. These are compared with the experimental measurements by Reibert (1996) and Reibert *et al.* (1996) and the FRNT results by Ng & Crouch (1999), where the disturbance amplitude A_s defined in (3.15) and in appendix A is used to quantify the receptivity.

5.1. Direct numerical simulations

The DNS solution presented in figure 8 is obtained for $Re_c = 2.4 \times 10^6$, $L_r = 12$ mm, $\varepsilon_r = 6$ μ m, $d_r = 3.7$ mm and $x_r/c = 0.023$. Because this configuration has been studied by all methods (experiment, DNS, PSE, FRNT: see table 1), it will serve as a reference case here. Numerical convergence of the DNS results has been ensured by a grid study, where the spectral order of the mesh ($N = 13$ instead of 11) and the location of the inflow plane ($3.6d_r$ instead of $4.6d_r$ upstream of the roughness) have been varied. The results (disturbance amplitudes, pressure coefficients) are identical

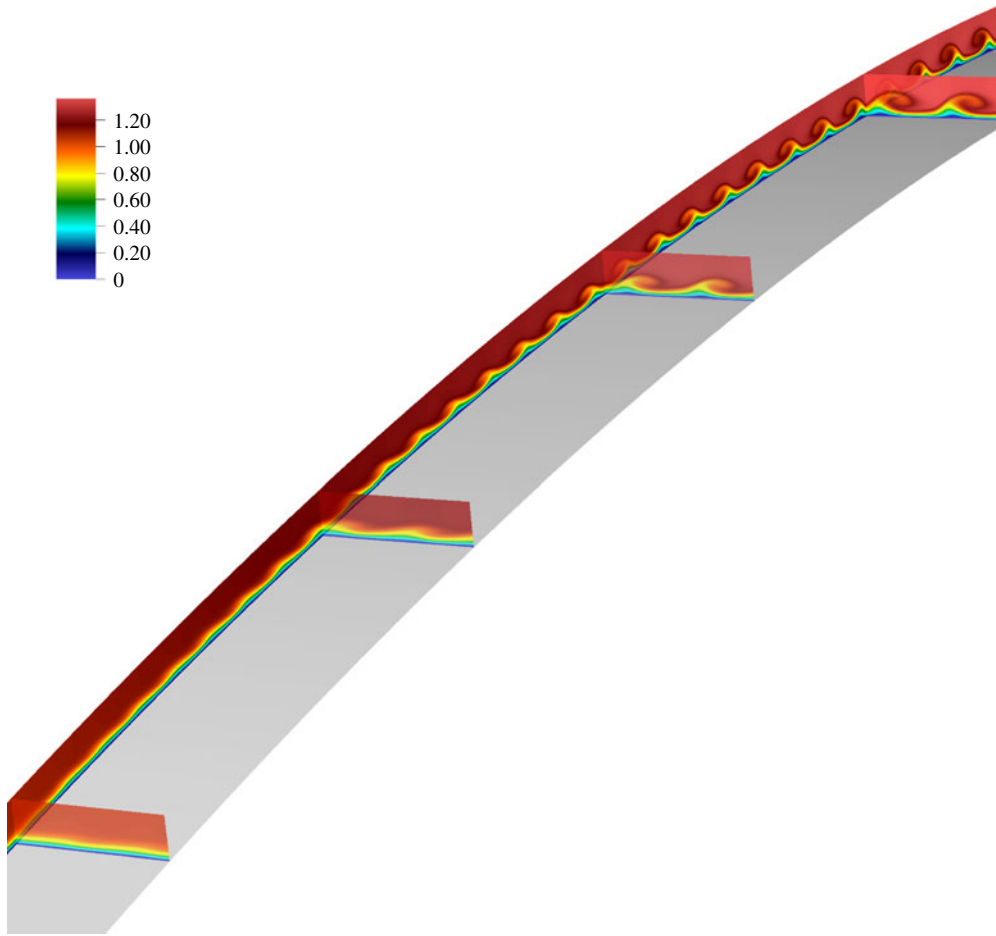


FIGURE 8. Planes of the total velocity field $U + u'$ as predicted by DNS for $Re_C = 2.4 \times 10^6$, $L_r = 12$ mm, $\varepsilon_r = 6$ μ m and $x_r/c = 0.023$. The cylindrical roughness element at $x_r/c = 0.023$ is meshed. The four spanwise slices of pseudocolours are located at $x/c = 0.25, 0.35, 0.45, 0.55$.

for all cases. Initial attempts involved polynomial orders of $N = 7$ and $N = 9$ but led to numerical instabilities, whereas computations with $N > 13$ become unfeasible. Figure 8 depicts various planes of the total velocity ($U + u'$) extracted from the flow field downstream of the meshed cylindrical roughness element (see § 3.1.2). Spanwise variations of the flow field become apparent for $x/c > 0.25$, suggesting that the excited disturbance has reached an amplitude of the order of the baseflow at this location. The flow structures that become clearly visible for $x/c > 0.35$ are characteristic of crossflow disturbances and conform to those observed by Reibert *et al.* (1996) and Haynes & Reed (2000).

The quantitative comparison with the experiments requires the extraction of the disturbance amplitude A_s , obtained from the DNS data by means of a fast Fourier transform in the spanwise direction. It turns out that the disturbance amplitude of the fundamental mode ($\lambda_z = 12$ mm) predicted by DNS is lower than that extracted

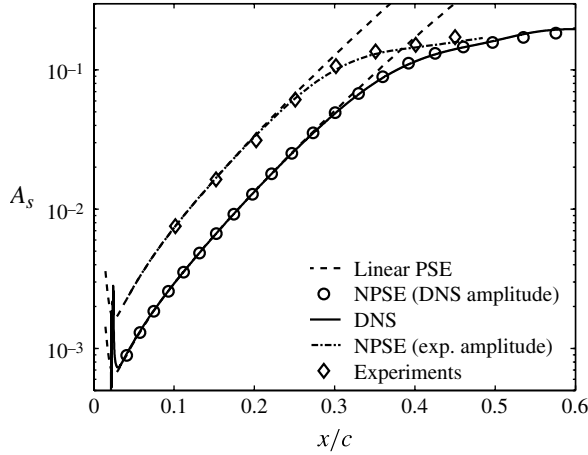


FIGURE 9. Disturbance amplitudes A_s of the crossflow mode with $\beta_0 = 2\pi/L_r$ extracted from DNS and experiments for $Re_c = 2.4 \times 10^6$, $L_r = 12$ mm, $\varepsilon_r = 6$ μm and $x_r/c = 0.023$. Further, amplitude evolutions predicted by NPSEs and the growth computed using linear PSEs are presented.

from the experiments by Reibert *et al.* (1996) (see figure 9). In the region of linear disturbance evolution, the DNS solution exhibits amplitudes which are 40% of those in the experiments. A comparison between results from DNS and linear PSEs shows that nonlinear effects become apparent at 29% chord, as opposed to the experimental measurements where saturation sets in at $\sim 22\%$ chord. However, the initial linear disturbance evolution predicted by DNS is in excellent agreement with the experimental observations, as can be seen by comparing with the corresponding linear PSE curves. In order to illuminate possible reasons for the different amplitude levels of DNS and experiment, we have also carried out an NPSE calculation, initializing the fundamental mode ($\beta_0 = 2\pi/L_r$) with the amplitude extracted from the DNS field at $x_r/c = 0.038$. The NPSE code encompasses the generation of harmonics by nonlinear interaction of the fundamental disturbance, and accounts for the contribution of the harmonics to the total disturbance once their amplitude exceeds a threshold of 10^{-9} (i.e. the harmonics need not necessarily be initialized). Here, a total number of 9 harmonics have been accounted for. The NPSE prediction perfectly matches the DNS amplitude, while favourable agreement with the experimental result is obtained, if the NPSEs are solved using an initial amplitude 2.5 times higher.

In figure 10, the DNS amplitudes of the fundamental mode β_0 and the superharmonics ($2\beta_0, 3\beta_0$) are compared with the corresponding NPSE results. Apart from the NPSE computation described above, where only the fundamental mode has been initiated, an additional NPSE calculation has been carried out, where the first two superharmonics ($2\beta_0, 3\beta_0$) are also initialized at $x/c = 0.038$ by the corresponding amplitudes extracted from the DNS solution. The purpose of this second NPSE computation is to include the roughness-induced receptivity of the superharmonics seen in the DNS. This allows us to distinguish between the contributions of receptivity and nonlinear interaction to the total disturbance amplitudes of the superharmonics.

Figure 10 reports that both NPSE computations accurately predict the amplitude evolution of the fundamental mode and the final amplitudes of both superharmonics. This shows that nonlinear interactions, forcing harmonic disturbances, determine the

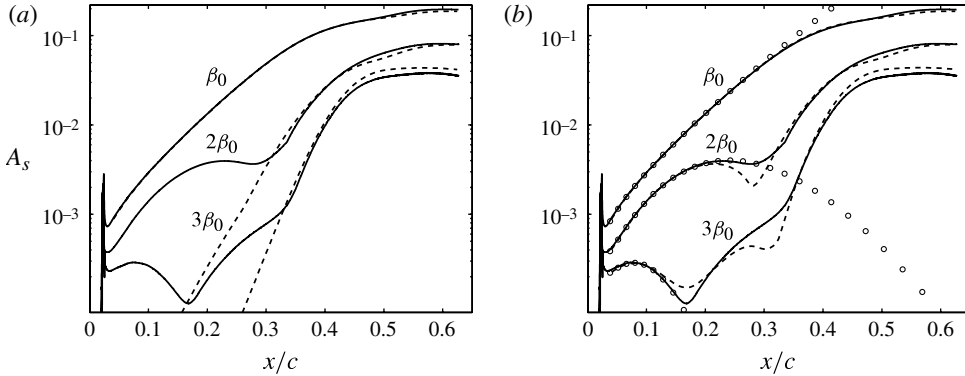


FIGURE 10. Disturbance amplitudes A_s of the fundamental mode $\beta_0 = 2\pi/L_r$ and the first two superharmonics ($2\beta_0, 3\beta_0$) as predicted by DNS (—) and NPSE (- - -), for $Re_C = 2.4 \times 10^6$, $L_r = 12$ mm, $\varepsilon_r = 6$ μ m and $x_r/c = 0.023$. (a) Only the fundamental mode was initiated. (b) All three modes were initiated at $x/c = 0.038$ when solving the NPSEs with amplitudes extracted from the DNS. Circles (\circ) denote the linear PSE solution.

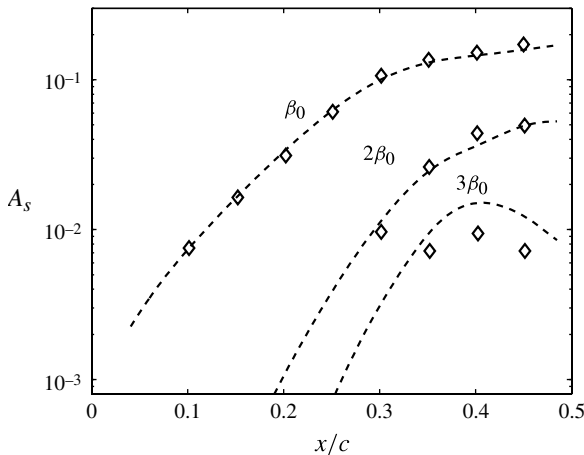


FIGURE 11. Disturbance amplitudes A_s of the fundamental mode β_0 and the first two superharmonics ($2\beta_0, 3\beta_0$) as predicted by NPSE (- - -) and extracted from the experiments (\diamond) for $Re_C = 2.4 \times 10^6$, $L_r = 12$ mm, $\varepsilon_r = 6$ μ m and $x_r/c = 0.023$. Only the fundamental mode was initiated when solving the NPSEs. Note that for β_0 the amplitude A_s is obtained according to (3.15) and the respective wall-normal position is denoted by η_{max,β_0} . For the superharmonics ($2\beta_0, 3\beta_0$) the amplitudes are defined by $A_s(\xi) = \hat{u}_s(\eta_{max,\beta_0}, \xi)$ in this figure.

final amplitudes of the superharmonics. The contribution due to receptivity becomes clear from figure 10(b), where both modes ($2\beta_0, 3\beta_0$) are seen to decay rather quickly once they are excited by the roughness element. Subsequently, both modes grow anew for $x/c > 0.3$ owing to nonlinear interaction. The discrepancies between the DNS and NPSE results of the superharmonics in the region $0.15 \leq x/c \leq 0.33$ might be due to additional non-modal growth effects in the DNS that are not included in the NPSE calculation.

The disturbance amplitudes of the ($\beta_0, 2\beta_0, 3\beta_0$) modes measured in the experiments are compared with NPSE predictions in figure 11. The NPSE result was obtained by

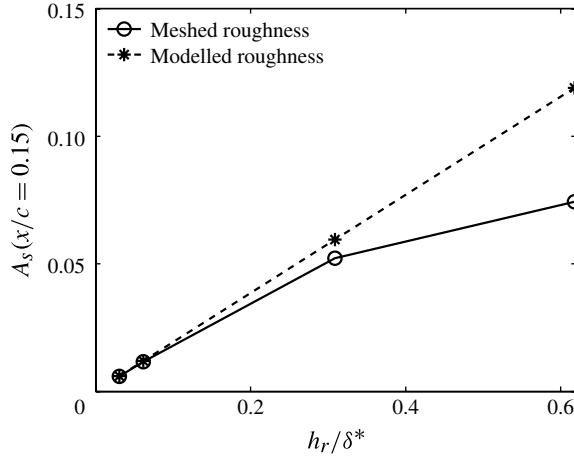


FIGURE 12. Disturbance amplitudes A_s at $x/c = 0.15$ obtained for simulations with either meshed roughness elements or the roughness model presented in § 3.1.2. $Re_C = 2.4 \times 10^6$, $L_r = 12$ mm, $x_r/c = 0.025$.

initiating the fundamental mode with an amplitude 2.5 times higher than that of the DNS, whereas the superharmonics were not initialized. It is apparent that both the fundamental mode amplitude and the amplitude evolution of the first superharmonic are well reproduced. This finding complies with results by Malik *et al.* (1999). The slight discrepancy in the amplitude of the second superharmonic $3\beta_0$ might be due to the limited accuracy in experimental measurements at such low amplitudes.

In addition to the reference case presented above, simulations for three different roughness heights have been performed using meshed roughness cylinders and the roughness model (see (3.2)), where the LNSEs have been solved in the latter case. Figure 12 shows the disturbance amplitudes obtained from both approaches (meshed and modelled roughness) for different roughness heights. The roughness height is varied between values of $0.03\delta_r^*$ and $0.6\delta_r^*$ (see table 1), where δ_r^* is the displacement thickness at the roughness position. The receptivity amplitude A_s obtained from the modelled roughness increases linearly with the roughness height, which is an inherent feature of the linear roughness model. The disturbance amplitude due to the meshed roughness elements increases nonlinearly with the roughness height and eventually becomes lower than the amplitudes obtained from the linear model. This trend towards saturation was also observed in the ASU experiments. For the two smallest roughness elements ($h_r = 0.03\delta_r^*$, $0.06\delta_r^*$) receptivity amplitudes obtained for the modelled roughness are in excellent agreement with those obtained for the meshed roughness. For roughness height $h_r = 0.3\delta_r^*$, the difference between the results obtained for meshed and modelled roughness elements already amounts to 14%, while the results differ by as much as 60% for the highest roughness ($h_r = 0.6\delta_r^*$). We conclude from our findings that the roughness model performs well for roughness heights below $\sim 10\%$ of the displacement thickness. Note that all roughness elements used in the experiments by Reibert *et al.* (1996) were lower than $0.1\delta_r^*$. It is therefore sufficient to employ the linear roughness model in LNSE simulations of the ASU experiments. The suitability of the linear roughness model demonstrated here is an important requirement for the application of PSE-based receptivity tools to the prediction of

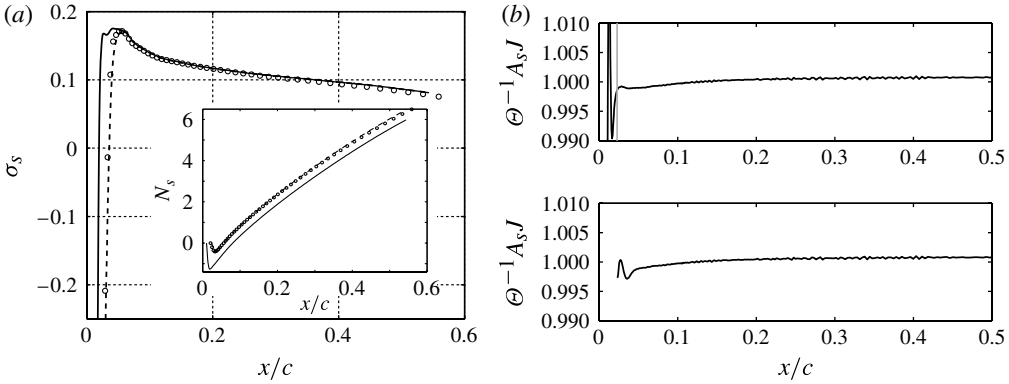


FIGURE 13. (a) N -factor $N = \log(A_s(\xi)/A_s(\xi_0))$ and growth rate $\sigma_s = \partial N/\partial \xi$ of crossflow mode with $\lambda_z = 12$ mm obtained by solving the PSEs. The PSEs have been initialized at $x_0/c = 0.01$ (—) and $x_0/c = 0.024$ (- - -). The circles denote a PSE solution about a baseflow computed using the c_p -distribution of the RANS flow field. (b) Comparison of the conservation of the left-hand-side of (3.9) for PSE solutions initiated at either $x_0/c = 0.01$ (upper figure) or $x_0/c = 0.024$ (lower figure). The vertical grey line denotes $x_r/c = 0.023$.

experimental results, because these tools build on such linear roughness models (see § 3.2.2).

5.2. Parabolized stability equations

Receptivity predictions based on the PSE approach (see § 3.2.2) are presented and compared with results from DNS and experiments. Further, we compare our work with results by Ng & Crouch (1999) based on local theory in order to highlight the influence of non-parallel effects on the receptivity amplitudes.

According to (3.14), the receptivity of a certain crossflow mode is obtained from a single solution of the direct and adjoint PSEs. A general issue when solving the PSEs is the initialization of the disturbance (see also Dobrinsky 2002). A common approach, followed here, is to initialize the PSEs at some upstream position x_0 by a solution to the local stability problem. In the case of crossflow modes, this approach leads to initial transient adjustments to the non-parallel flow. One example is reported in figure 13(a), where the evolution of a crossflow mode with $\lambda_z = 12$ mm is shown. The initial decay rates of the crossflow modes are $\sigma_s = -1.37$ and $\sigma_s = -0.32$ for positions $x_0/c = 0.01$ and $x_0/c = 0.024$ respectively. Here, growth rates are defined by $\sigma_s = \partial N/\partial \xi$, where the N -factor is $N = \log(A_s(\xi)/A_s(\xi_0))$. The PSE result obtained for two different initial positions is presented. It is apparent that the initial evolution of the crossflow mode is quite dependent on the position of initialization. Also, the first neutral point ($\sigma_s = 0$) of the crossflow mode is not well defined as it moves upstream for smaller values of x_0 . Eventually, the transient effects have decayed and the two solutions coincide, in this case for $x/c \geq 0.06$.

The conservation of the bilinear concomitant for the homogeneous case (see (3.9)) is shown in figure 13(b) for two direct/adjoint PSE solutions initiated at different positions. It becomes clear that, although much weaker when initiated at $x_0/c = 0.024$, both solutions exhibit transients which manifest themselves as oscillations of the concomitant. The transient oscillations disappear quickly and a smooth, well-conserved bilinear concomitant is obtained for the domain of interest, which guarantees accurate receptivity predictions. However, the farther upstream the crossflow mode is initiated

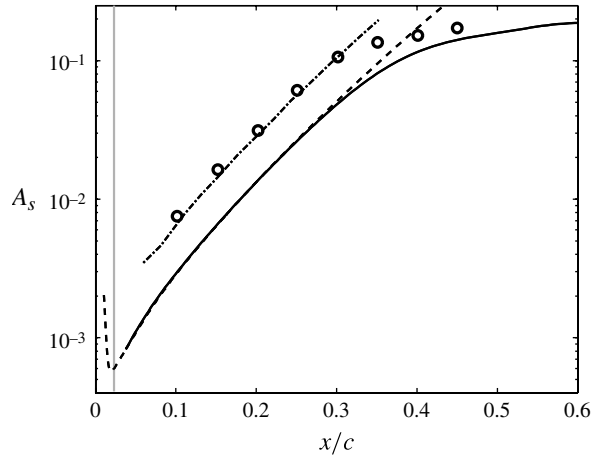


FIGURE 14. Disturbance amplitudes A_s of a crossflow mode with $\lambda_z = 12$ mm obtained from PSE (---), DNS (—), experiments (o), and FRNT (- · -). The grey vertical line denotes the roughness position $x/c = 0.023$. $Re_C = 2.4 \times 10^6$, $L_r = 12$ mm and $\varepsilon_r = 6$ μ m.

the earlier we obtain a smooth and conserved function. In order to avoid transient effects in the region of interest, the PSEs should therefore be initialized as far upstream as is possible, to identify discrete eigenmodes from the local stability solution. This practice has been adopted here, i.e. $x_0/c = 0.01$ is chosen for the 12 mm mode.

As mentioned earlier, the baseflow used for the PSE analyses was computed by solving the BLEs based on the pressure coefficient from DNS. However, the latter differed slightly from the experimental distribution, whereas we have obtained good agreement between the results from the RANS computation and the experiment (see figure 5). Therefore, in order to investigate the effect of a perturbation in c_p on the disturbance evolution, we have performed a PSE computation about a different baseflow, computed using the c_p distribution of the RANS flow field. Figure 13(a) shows that the effect on the spatial evolution of the crossflow mode is negligible. This justifies the use of the DNS-based pressure coefficient to solve the BLEs.

The crossflow amplitudes predicted by the PSE-based receptivity model for $Re_C = 2.4 \times 10^6$, $L_r = 12$ mm, $x/c = 0.023$ and $\varepsilon_r = 6$ μ m are presented in figure 14. They are compared with our DNS results, the experimental measurements by Reibert (1996) and the FRNT results by Ng & Crouch (1999). The amplitudes predicted by the PSE model are slightly higher ($\sim 1\%$) than those obtained from DNS, while the amplitudes predicted by Ng & Crouch (1999) based on FRNT are more than twice as large. In fact, the FRNT results agree much better with those from the experiment, but this appears to be fortuitous: it is well known that receptivity models based on the assumption of a locally parallel baseflow over-predict disturbance amplitudes (see e.g. Collis & Lele 1999), and here we arrive at the same conclusion when comparing the findings of Ng & Crouch (1999) with our DNS results.

In order to further validate the PSE-based receptivity model, additional direct numerical simulations have been carried out for different roughness positions. The amplitudes of the fundamental crossflow mode with $\beta_0 = 2\pi/L_r$ ($L_r = 12$ mm) and of the two superharmonics ($2\beta_0, 3\beta_0$) excited by the roughness disk are compared to PSE predictions in figure 15. The amplitudes are evaluated at positions where the crossflow

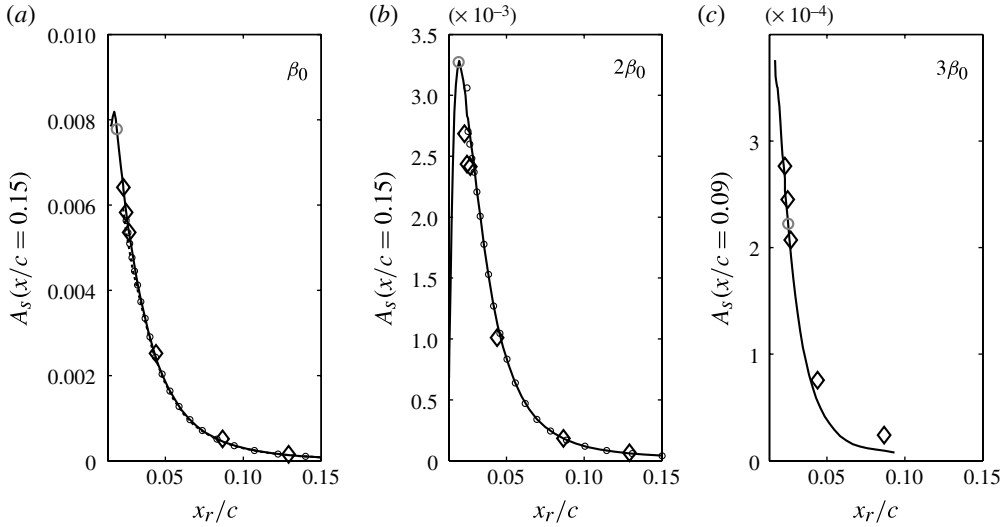


FIGURE 15. Amplitudes of crossflow modes excited at different roughness positions x_r and $Re_c = 2.4 \times 10^6$, $L_r = 12$ mm and $\varepsilon_r = 6$ μ m. (a) Fundamental mode with $\beta_0 = 2\pi/L_r$ as predicted by DNS (\diamond) and PSE methods. The PSEs have been initialized at $x_0/c = 0.01$ (—) and $x_0/c = 0.024$ (small circles \circ). (b) Superharmonic with $2\beta_0$ as predicted by DNS (\diamond) and PSE methods. The PSEs have been initialized at $x_0/c = 0.01$ (—) and $x_0/c = 0.024$ (small circles \circ). (c) Superharmonic with $3\beta_0$ as predicted by DNS (\diamond) and PSEs initialized at $x_0/c = 0.015$ (—). The dashed line (—) in (a) denotes solutions obtained for a baseflow computed based on c_p extracted from the RANS solution. The grey circles in (a–c) denote the first neutral points of the respective crossflow modes.

disturbances evolve linearly and are clearly distinguishable in the DNS data. For the β_0 and $2\beta_0$ modes, $x/c = 0.15$ is an appropriate choice, whereas $x/c = 0.09$ is chosen for the $3\beta_0$ mode. The amplitude prediction based on the PSEs is in good agreement with the DNS solution for all three crossflow modes. In general, we observe maximum receptivity upstream of – but very close to – the first neutral point of the crossflow modes. This was also found by Ng & Crouch (1999). Downstream of the neutral point, the receptivity decreases monotonically for increasing roughness positions. Although the initial phase of the crossflow modal evolution predicted by PSEs strongly depends on the position x_0 of the initialization of the disturbance (see figure 13a), the receptivity predicted by PSEs does not depend on x_0 , as shown in figure 15 for the fundamental mode and the first harmonic. This is not surprising, as the receptivity is mainly evaluated from the solution of the adjoint PSEs (see (3.14)), which is barely affected by the position of the initialization of the direct PSEs. As shown earlier in figure 13, the crossflow mode evolution is insensitive to slight changes in the pressure coefficient of the baseflow, and here, figure 15(a) demonstrates that this also holds true for the receptivity: the amplitude of the fundamental crossflow mode is hardly affected when computed for the baseflow deduced from the c_p -distribution of the RANS flow field.

Figure 15 clearly demonstrates the strong sensitivity of the receptivity amplitude of the steady crossflow mode and its superharmonics to the chordwise location of the roughness cylinder, where already a moderate upstream shift of the roughness element leads to a dramatic increase of the receptivity. The additional receptivity of

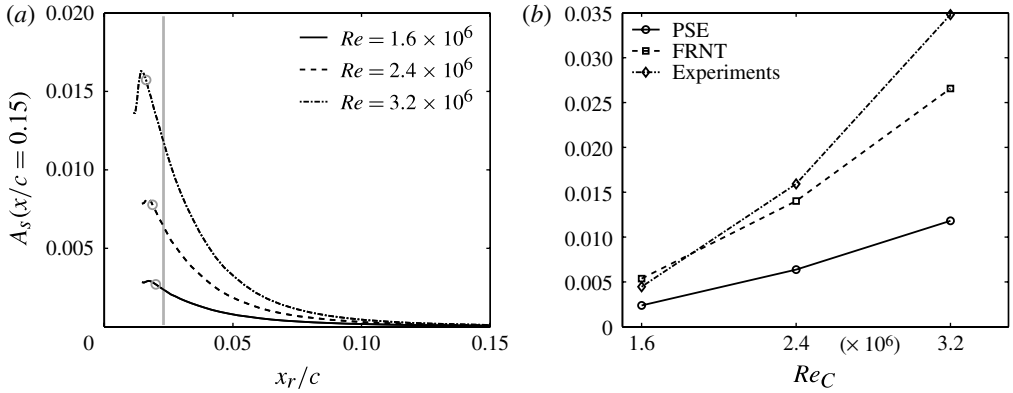


FIGURE 16. Disturbance amplitudes of crossflow modes with $\lambda_z = 12$ mm for different Reynolds numbers and $\varepsilon_r = 6$ μm , $d_r = 3.7$ mm, $L_r = 12$ mm. (a) Amplitudes predicted by PSE versus roughness position x_r . Grey circles denote the first neutral point of the respective crossflow mode and the grey vertical line denotes $x_r/c = 0.023$. (b) Amplitudes for $x_r/c = 0.023$ obtained from experiments and predicted by the PSE and FRNT methods.

the experiments as compared to our DNS may hence be partly caused by a slight misplacement of the roughness array on the wind tunnel wing model.

The success of the PSE-based receptivity model demonstrated here as well as by Chang & Choudhari (2005), for example, suggests employing it for additional cases at different Reynolds numbers considered in the experiments by Reibert (1996). Ng & Crouch (1999) reported an increasing discrepancy between their FRNT results and those from the ASU experiments for increasing Reynolds numbers. This is also true for the present PSE-predicted amplitudes, as seen in figure 16(b). In general, the receptivity amplitudes increase for larger values of Re_C . As expected, the PSE-predicted amplitudes are lower than those measured by Reibert (1996) and those predicted by the FRNT. For $Re_C = 1.6 \times 10^6$, the PSE and experimental results differ by a factor of 1.9, and for $Re_C = 3.2 \times 10^6$ the difference has increased to a factor of 2.8.

Next, we investigate the effect of roughness element spacing by considering a value of $L_r = 36$ mm instead of 12 mm. The receptivity results for the first three harmonics are presented in figure 17. Maximum receptivity is again found slightly upstream of the first neutral point, while the receptivity decreases farther downstream. Figure 17 also reports that the receptivity increases for smaller wavelengths. It is interesting to note that, once the PSE-predicted amplitudes are multiplied by a factor of 2.9, they nearly coincide with the experimental measurements for all wavelengths. Note, that this factor is still in the range of linear receptivity. This is a strong indicator of additional receptivity in the experiments: either the roughness cylinders were higher than the nominal value of 6 μm given by Reibert (1996), or additional natural roughness was present in the leading-edge region. Indeed, Reibert (1996) stated that ‘[...] the surface of the element is somewhat uneven’. The existence of background noise in the wind tunnel free stream, on the other hand, can be discarded as a reason for the discrepancy between our results and those by Reibert (1996), because free-stream turbulence would most probably not force stationary modes of different wavelength equally.

The contribution of hypothetical natural leading-edge roughness to the larger receptivity observed in the experiments is studied next. Since natural roughness is

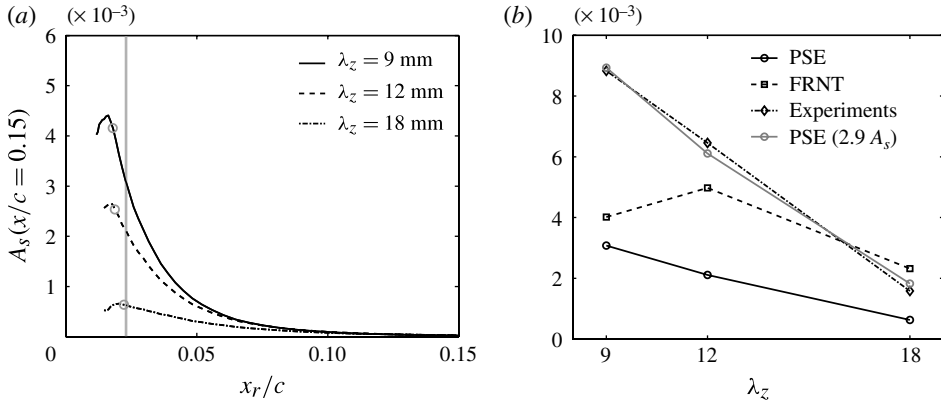


FIGURE 17. Disturbance amplitude of crossflow modes excited by roughness cylinders with a spacing of $L_r = 36$ mm and $\varepsilon_r = 6$ μm , $d_r = 3.7$ mm. The Reynolds number was $Re_C = 2.4 \times 10^6$. (a) Amplitudes versus roughness position predicted by the PSE method. Grey circles denote the respective first neutral point. The grey vertical line denotes $x_r/c = 0.023$. (b) Amplitudes for $x_r/c = 0.023$ versus λ_z as predicted by the PSE and FRNT methods and obtained from experiments.

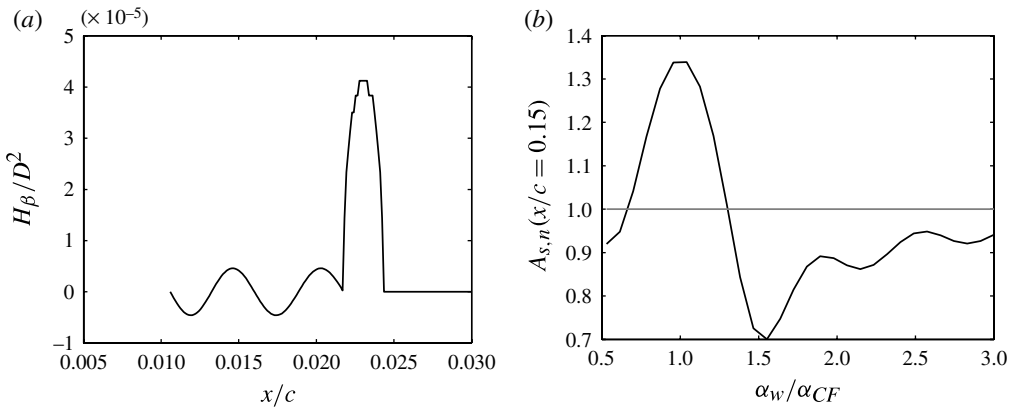


FIGURE 18. (a) Geometry function H_β for a combination of a wavy wall ($\alpha_w/\alpha_{CF} = 1.3$) upstream of a roughness cylinder. The roughness cylinder considered is defined by $L_r = 12$ mm, $\varepsilon_r = 6$ μm , $d_r = 3.7$ mm, $x_{r,cyl}/c = 0.023$ and $\beta = 2\pi/L_r$. (b) Disturbance amplitude of a $\lambda_z = 12$ mm crossflow mode versus the wall wavenumber α_w obtained for $Re_C = 2.4 \times 10^6$. The disturbance amplitude $A_{s,n}$ is normalized with the amplitude obtained when only the roughness cylinder is considered.

inherently random in space, it is difficult to model its effect on receptivity. Here, an attempt is made to investigate the effects of non-localized roughness upstream of the localized cylindrical elements, using a simple model of distributed roughness. To this end, a wavy wall is chosen for the non-localized roughness region, as illustrated in figure 18(a). The wavy wall extends from the location x_0 , where the PSEs are initiated, to the position of the roughness cylinder. Various wavy walls with chordwise wavenumbers in the range from $0.5\alpha_{CF}$ to $3\alpha_{CF}$ are considered, where α_{CF} denotes

the real part of the tangential crossflow wavenumber at the roughness position. The roughness height has been chosen to correspond to the roughness r.m.s. level $0.25 \mu\text{m}$ apparent in the leading-edge region of the experimental wing model (see Reibert 1996). The roughness cylinder downstream of the wavy surface is defined by $L_r = 12 \text{ mm}$, $\varepsilon_r = 6 \mu\text{m}$, $d_r = 3.7 \text{ mm}$, $x_{r,\text{cyl}}/c = 0.023$. The disturbance amplitudes obtained are presented in figure 18(b). They are normalized by the amplitude obtained in the absence of the wavy wall (see figure 16b). The variation of the disturbance amplitudes with respect to different values of α_r is due to phase differences of the excited crossflow modes. It is apparent that the effect of wavy low-amplitude wall roughness upstream of the roughness cylinder can be significant. Compared with results obtained with the localized roughness cylinder alone, disturbance amplitudes can vary by more than 50%. Hence, non-localized natural roughness upstream of the localized roughness cylinder could explain differences between theory, simulations and experiments. On the other hand, we have demonstrated that the difference between our results and those by Reibert (1996) is manifested by a nearly constant factor around 2.9, irrespective of the crossflow modal wavelength. It is hard to believe that natural random roughness affects all disturbance modes similarly.

6. Conclusions

The receptivity of a swept-wing boundary layer to localized surface roughness is studied by DNS and calculations using the PSE method. The flow configuration considered models wind tunnel experiments by Reibert *et al.* (1996), where a spanwise array of micron-sized cylinders was placed near the leading edge of the wing in order to excite steady crossflow modes. The roughness array is implemented in the DNS as a single cylinder combined with cyclic boundary conditions, accounting for the spanwise periodic row of roughness elements used in the experiments. Apart from a meshed roughness cylinder, we consider a linear roughness model mimicking the effect of the cylinder on the flow field by inhomogeneous velocity boundary conditions at the undisturbed wall. This treatment of the roughness is also combined with a receptivity model based on the direct and adjoint PSEs, which fully accounts for the non-parallel spatial evolution of the swept-wing boundary layer.

Results are as follows. The amplitude of the crossflow mode excited by the linear roughness model agrees favourably with that obtained with the meshed roughness unless the roughness height exceeds a level of $\sim 10\%$ of the displacement thickness. Above this threshold, nonlinear effects on the receptivity are no longer negligible. We also demonstrate by DNS and the PSE-based receptivity model that the receptivity amplitude of the steady crossflow mode is sensitive to the chordwise location of the roughness cylinder, where a moderate upstream shift leads to a significant increase of the disturbance amplitudes. For all roughness locations tested, the maximum difference between the fundamental mode amplitudes predicted by the receptivity model and those from the DNS is $\sim 10\%$. For roughness positions which are close to the experimental position the difference is of order 1%. This establishes a considerable improvement compared to receptivity prediction tools using the FRNT on the grounds of the parallel flow assumption. We find that the results from the receptivity model are insensitive to the position of initialization of the PSEs, furnishing the model with robustness and reliability. The receptivity model is also efficient and versatile, as one single solution of the combined direct/adjoint PSE system is sufficient to determine receptivity amplitudes for arbitrary roughness shapes and positions.

The agreement between numerical and experimental results, on the other hand, is less close. For a Reynolds number of $Re_C = 2.4 \times 10^6$, the crossflow modal amplitude extracted from our DNS data is 40% of that measured by Reibert *et al.* (1996). We notice a significant improvement compared with the DNS study by T. Nishino and K. Shariff (personal communication), where the amplitude of the crossflow mode differed from the experimental value by one order of magnitude. These authors attributed this significant difference to an insufficient grid resolution or the use of a square roughness shape instead. Neither deficiency is present in the current study as we present a well-resolved DNS using the correct roughness shape. Supplementary linear and NPSE calculations reveal that the linear spatial evolution of the steady crossflow mode from the DNS and experimental data is in good agreement, i.e. the discrepancy can be entirely attributed to additional receptivity in the experiments. This is further substantiated by consulting the PSE-based receptivity model for an additional case studied experimentally by Reibert (1996) exhibiting a different spacing of the roughness cylinders. It turns out that the PSE-predicted disturbance amplitudes of the roughness-induced crossflow modes is consistently lower by a factor of 2.9 than those from the experimental measurements, irrespective of the spanwise wavelength of the disturbance. This fact suggests that uncontrolled noise such as free-stream turbulence and natural surface roughness is most probably not accountable for the additional receptivity in the experiments. Although supplementary PSE computations with a localized wavy roughness upstream of the cylinder indicate that leading-edge roughness can cause an increase of the total receptivity, it is hard to believe that natural roughness of random spatial distribution would enhance the receptivity of one single mode by the same amount. We therefore conjecture that the discrepancy is more likely related to an experimental uncertainty of the roughness height, inaccuracies of the mounting of the micro-cylinders, or a combination of both. A slightly shorter distance between the row of roughness elements and the leading edge and somewhat higher roughness cylinders might have caused the additional receptivity observed in the experiments.

Acknowledgements

The authors wish to thank W. Saric and M. Reibert for providing the experimental pressure data. Computer time provided by SNIC (Swedish National Infrastructure for Computing) at the Center for Parallel Computers (PDC), KTH, and at the National Supercomputer Centre (NSC), Linköping University, is gratefully acknowledged.

Appendix A. Disturbance amplitudes

A quantitative comparison with experimental results requires the extraction of disturbance amplitudes from DNS/PSE solutions. As mentioned in § 2.1, the numerical and experimental amplitudes compared here are based on slightly different velocity profiles, i.e. $\hat{u}_{s,n}$ and $\hat{u}_{s,e}$ respectively. The disturbance amplitudes obtained from DNS and PSE solutions are presented as

$$A_s = \max_{\eta} \frac{|\hat{u}_{s,n}|}{\sqrt{2}}, \quad (\text{A1})$$

with

$$\hat{u}_{s,n} = \hat{u}_{\xi} \cos \phi_0 + \hat{w} \sin \phi_0. \quad (\text{A2})$$

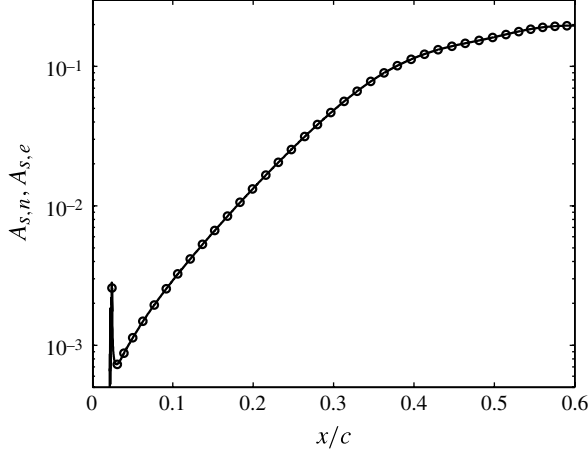


FIGURE 19. Comparison of disturbance amplitudes evaluated on the basis of $u_{s,n}$ (—) as well as $u_{s,e}$ (○).

The experimental amplitudes A_s used by Reibert (1996) are based on the total velocity in the s -plane, $\hat{u}_{s,e}$, while the latter is a function of $Y = \underline{y} - \underline{y}_{wall}$. Hence,

$$A_s = \max_Y \frac{|\hat{u}_{s,e}|}{\sqrt{2}}. \quad (\text{A } 3)$$

In figure 19 it becomes clear that the two definitions yield very similar amplitudes, i.e. the influence of both the wall-normal velocity component and the difference between the η - and \underline{y} -coordinate is negligible. This justifies the practice adopted in this article to directly compare disturbance amplitudes obtained from slightly different definitions.

Appendix B. PSE operators

In § 5.2 the PSEs are expressed in operator form as

$$\mathcal{L} \mathbf{q} = 0, \quad (\text{B } 1)$$

with \mathcal{L} being a linear operator of the form

$$\mathcal{L} = \mathbf{A} + \mathbf{B} \frac{\partial}{\partial \eta} + \mathbf{C} \frac{\partial^2}{\partial \eta^2} + \mathbf{D} \frac{1}{h_1} \frac{\partial}{\partial \xi} \quad (\text{B } 2)$$

and $\mathbf{q} = (u, v, w, p)^T$ representing the state vector. The scaling factor h_1 is defined by $h_1^2 = \sum_{j=1}^3 (\partial x_j / \partial \xi)^2$, where x_j represents the Cartesian coordinates of the reference system. The individual linear operators \mathbf{A} , \mathbf{B} , \mathbf{C} and \mathbf{D} take the form

$$\mathbf{A} = \begin{pmatrix} i\alpha_0 & m_{12} & i\beta & 0 \\ C + \partial U_\xi / \partial \xi & \partial U_\xi / \partial \eta + m_{12} U_\xi & 0 & i\alpha_0 \\ -2m_{12} U_\xi & C + \partial V_\eta / \partial \eta & 0 & 0 \\ \partial W / \partial \xi & \partial W / \partial \eta & C & i\beta \end{pmatrix}, \quad (\text{B } 3)$$

$$\mathbf{B} = \begin{pmatrix} 0 & 1 & 0 & 0 \\ V_\eta & 0 & 0 & 0 \\ 0 & V_\eta & 0 & 1 \\ 0 & 0 & V_\eta & 0 \end{pmatrix}, \quad (\text{B } 4)$$

$$\mathbf{C} = \begin{pmatrix} 0 & 0 & 0 & 0 \\ -\frac{1}{Re} & 0 & 0 & 0 \\ 0 & -\frac{1}{Re} & 0 & 0 \\ 0 & 0 & -\frac{1}{Re} & 0 \end{pmatrix}, \quad (\text{B } 5)$$

$$\mathbf{D} = \begin{pmatrix} 1 & 0 & 0 & 0 \\ U_\xi & 0 & 0 & 0 \\ 0 & U_\xi & 0 & 0 \\ 0 & 0 & U_\xi & 0 \end{pmatrix}, \quad (\text{B } 6)$$

where

$$\alpha_0 = \frac{\alpha}{h_1}, \quad (\text{B } 7)$$

$$m_{12} = \frac{1}{h_1} \frac{\partial h_1}{\partial \eta}, \quad (\text{B } 8)$$

$$C = -i\omega + i\alpha_0 U_\xi + i\beta W + \frac{1}{Re}(\alpha_0^2 + \beta^2). \quad (\text{B } 9)$$

Appendix C. Lagrange identity

In § 3.2.2 the receptivity of a disturbance to inhomogeneous boundary conditions is determined via a Lagrange identity of the form

$$\langle \mathbf{q}^*, \mathcal{L}\mathbf{q} \rangle = \langle \mathcal{L}^*\mathbf{q}^*, \mathbf{q} \rangle + \iint_\Omega \nabla \cdot \mathcal{J}(\mathbf{q}, \mathbf{q}^*) h_1 d\xi d\eta, \quad (\text{C } 1)$$

where $\mathcal{L}\mathbf{q}$ denote the direct PSEs. The adjoint PSEs represented by $\mathcal{L}^*\mathbf{q}^*$ and the bilinear concomitant \mathcal{J} are obtained by performing integration by parts on the leftmost inner product in (C 1) yielding

$$\begin{aligned} & \iint_\Omega (\mathbf{q}^*)^H \left(\mathbf{A}\mathbf{q} + \mathbf{B}\frac{\partial \mathbf{q}}{\partial \eta} + \mathbf{C}\frac{\partial^2 \mathbf{q}}{\partial \eta^2} + \mathbf{D}\frac{1}{h_1}\frac{\partial \mathbf{q}}{\partial \xi} \right) h_1 d\xi d\eta \\ &= \iint_\Omega \left(\mathbf{A}^*\mathbf{q}^* + \mathbf{B}^*\frac{\partial \mathbf{q}^*}{\partial \eta} + \mathbf{C}^*\frac{\partial^2 \mathbf{q}^*}{\partial \eta^2} + \mathbf{D}^*\frac{1}{h_1}\frac{\partial \mathbf{q}^*}{\partial \xi} \right)^H \mathbf{q} h_1 d\xi d\eta \\ &+ \int_{\xi_0}^{\xi_1} \left[(\mathbf{q}^*)^H \left(\mathbf{B} - \frac{\partial \mathbf{C}}{\partial \eta} - m_{12}\mathbf{C} \right) \mathbf{q} + (\mathbf{q}^*)^H \mathbf{C} \frac{\partial \mathbf{q}}{\partial \eta} - \left(\frac{\partial \mathbf{q}^*}{\partial \eta} \right)^H \mathbf{C} \mathbf{q} \right]_{\eta=0}^{\eta=\infty} h_1 d\xi \\ &+ \int_0^\infty [(\mathbf{q}^*)^H \mathbf{D} \mathbf{q}]_{\xi_0}^{\xi_1} d\eta, \end{aligned} \quad (\text{C } 2)$$

with

$$\mathbf{A}^* = \mathbf{A}^H - \frac{\partial \mathbf{B}^H}{\partial \eta} - m_{12} \mathbf{B} + \frac{\partial^2 \mathbf{C}^H}{\partial \eta^2} + 2m_{12} \frac{\partial \mathbf{C}^H}{\partial \eta} - \frac{\partial \mathbf{D}^H}{\partial \xi}, \quad (\text{C3})$$

$$\mathbf{B}^* = -\mathbf{B}^H + 2 \frac{\partial \mathbf{C}^H}{\partial \eta} + 2m_{12} \mathbf{C}^H, \quad (\text{C4})$$

$$\mathbf{C}^* = \mathbf{C}^H, \quad (\text{C5})$$

$$\mathbf{D}^* = -\mathbf{D}^H. \quad (\text{C6})$$

The bilinear concomitant \mathcal{J} thus takes the form

$$\mathcal{J}(1) = \frac{1}{h_1} (\mathbf{q}^*)^H \mathbf{D} \mathbf{q}, \quad (\text{C7})$$

$$\mathcal{J}(2) = (\mathbf{q}^*)^H \left(\mathbf{B} - \frac{\partial \mathbf{C}}{\partial \eta} - m_{12} \mathbf{C} \right) \mathbf{q} + (\mathbf{q}^*)^H \mathbf{C} \frac{\partial \mathbf{q}}{\partial \eta} - \left(\frac{\partial \mathbf{q}^*}{\partial \eta} \right)^H \mathbf{C} \mathbf{q}, \quad (\text{C8})$$

$$\mathcal{J}(3) = 0. \quad (\text{C9})$$

REFERENCES

- AIRIAU, C. 2000 Non-parallel acoustic receptivity of a Blasius boundary layer using an adjoint approach. *Flow Turbul. Combust.* **65**, 347–367.
- AIRIAU, C., WALTHER, S. & BOTTARO, A. 2002 Boundary layer sensitivity and receptivity. *C. R. Mécanique* **330**, 259–265.
- ANDERSSON, P., HENNINGSON, D. S. & HANIFI, A. 1998 On a stabilization procedure for the parabolic stability equations. *J. Engng Math.* **33** (3), 311–332.
- BERTOLOTTI, F. P. 2000 Receptivity of three-dimensional boundary-layers to localized wall roughness and suction. *Phys. Fluids* **12** (7), 1799–1809.
- BERTOLOTTI, F. P., HERBERT, T. & SPALART, P. R. 1992 Linear and nonlinear stability of the Blasius boundary layer. *J. Fluid Mech.* **242**, 441–474.
- BIPES, H. 1999 Basic experiments on transition in three-dimensional boundary layers dominated by crossflow instability. *Prog. Aerosp. Sci.* **35**, 363–412.
- CARPENTER, A. L., SARIC, W. S. & REED, H. L. 2009 In-flight receptivity experiments on a 30-degree swept-wing using micron-sized discrete roughness size influence. *AIAA Paper* 2009-590.
- CARPENTER, M. H., CHOUDHARI, M., LI, F., STRETT, C. L. & CHANG, C.-L. 2010 Excitation of crossflow instabilities in a swept wing boundary layer. *AIAA Paper* 2010-378.
- CHANG, C.-L. & CHOUDHARI, M. 2005 Boundary-layer receptivity and integrated transition prediction. *AIAA Paper* 2005-0526.
- CHANG, C.-L., MALIK, M. R., ERLEBACHER, G. & HUSSAINI, M. Y. 1991 Compressible stability of growing boundary layers using parabolized stability equations. *AIAA Paper* 1991-1636.
- CHOUDHARI, M. 1994 Roughness-induced generation of crossflow vortices in three-dimensional boundary layers. *Theoret. Comput. Fluid Dyn.* **6**, 1–30.
- COLLIS, S. S. & LELE, S. K. 1999 Receptivity to surface roughness near a swept leading edge. *J. Fluid Mech.* **380**, 141–168.
- CROUCH, J. D. 1993 Receptivity of three-dimensional boundary layers. *AIAA Paper* 93-0074.
- DEYHLE, H. & BIPES, H. 1996 Disturbance growth in an unstable three-dimensional boundary layer and its dependence on environmental conditions. *J. Fluid Mech.* **316**, 73–113.
- DOBRINSKY, A. 2002 Adjoint analysis for receptivity prediction. PhD thesis, Rice University.
- ELIASSON, P. 2002 EDGE: a Navier–Stokes solver for unstructured grids. In *Proceedings to Finite Volumes for Complex Applications III* (ed. D. Kroner & R. Herbin), pp. 527–534. Hemre Penton Science London.

- FEDOROV, A. V. 1988 Excitation of waves of instability of the secondary flow in the boundary layer on a swept wing. *J. Appl. Mech. Tech. Phys.* **29**, 643–648.
- FISCHER, P. F., LOTTES, J. W. & KERKEMEIER, S. G. 2008 Nek5000 Web page. <http://nek5000.mcs.anl.gov>.
- HAJ-HARIRI, H. 1994 Characteristics analysis of the parabolized stability equations. *Stud. Appl. Math.* **92**, 41–53.
- HANIFI, A., HENNINGSON, D. S., HEIN, S., BERTOLOTTI, F. P & SIMEN, M. 1994 Linear non-local instability analysis: the linear NOLOT code. *FFA TN* 1994-54.
- HANIFI, A., SCHMID, P. J. & HENNINGSON, D. S. 1996 Transient growth in compressible boundary layer flow. *Phys. Fluids* **8** (3), 826–837.
- HAYNES, T. S. & REED, H. L. 2000 Simulation of swept-wing vortices using nonlinear parabolized stability equations. *J. Fluid Mech.* **405**, 325–349.
- HEIN, S., HANIFI, A. & CASALIS, G. 2000 Nonlinear transition prediction. In *Proceedings of the European Congress on Computational Methods in Applied Sciences and Engineering*.
- HELLSTEN, A. 2005 New advanced k - ω turbulence model for high-lift aerodynamics. *AIAA J.* **43** (9), 1857–1869.
- HERBERT, T. 1997 Parabolized stability equations. *Annu. Rev. Fluid Mech.* **29**, 245–283.
- HILL, D. C. 1995 Adjoint systems and their role in the receptivity problem for boundary layers. *J. Fluid Mech.* **292**, 183–204.
- HILL, D. C. 1997 Receptivity in non-parallel boundary layers. In *Proceedings of the 1997 ASME Fluids Engineering Division Summer Meeting*. ASME.
- MADAY, Y. & PATERA, A. T. 1989 Spectral element methods for the Navier–Stokes equations. In *State of the Art Surveys in Computational Mechanics* (ed. A. K. Noor). pp. 71–143. ASME.
- MALIK, M. R., LI, F., CHOUDHARI, M. M. & CHANG, C.-L. 1999 Secondary instability of crossflow vortices and swept-wing boundary-layer transition. *J. Fluid Mech.* **399**, 85–115.
- MANUILOVICH, S. V. 1989 Disturbances of a three-dimensional boundary layer generated by surface roughness. *Fluid Dyn.* **24**, 764–769.
- NG, L. L. & CROUCH, J. D. 1999 Roughness-induced receptivity to crossflow vortices on a swept wing. *Phys. Fluids* **11** (2), 432–438.
- NISHINO, T. & SHARIFF, K. 2009 Direct numerical simulation of a swept-wing boundary layer with an array of discrete roughness elements. In *Proceedings 7th IUTAM Symposium on Laminar-Turbulent Transition, Stockholm, Sweden*. Springer.
- OHLSSON, J., SCHLATTER, P., FISCHER, P. F. & HENNINGSON, D. S. 2011 Stabilization of the spectral-element method in turbulent flow simulations. In *Spectral and High Order Methods for Partial Differential Equations* (ed. J. S. Hesthaven & E. M. Rønquist), pp. 449–458. Springer.
- PATERA, A. T. 1984 A spectral element method for fluid dynamics: laminar flow in a channel expansion. *J. Comput. Phys.* **54**, 468–488.
- PIOT, E., CONTENT, C. & CASALIS, G. 2008 Receptivity of crossflow instabilities to a periodic roughness array on a swept cylinder: investigation of the roughness size influence. *AIAA Paper* 2008-502.
- REIBERT, M. S. 1996 Nonlinear stability, saturation, and transition in crossflow-dominated boundary layers. PhD thesis, Arizona State University.
- REIBERT, M. S., SARIC, W. S., CARILLO, R. B. & CHAPMAN, K. L. 1996 Experiments in nonlinear saturation of stationary crossflow vortices in a swept-wing boundary layer. *AIAA Paper* 96-0184.
- RIZZETTA, D. P., VISBAL, M. R., REED, H. L. & SARIC, W. S. 2010 Direct numerical simulation of discrete roughness on a swept-wing leading edge. *AIAA J.* **48** (11).
- SAKOV, P. 2011 gridgen-c: an orthogonal grid generator based on the CRDT algorithm (by conformal mapping). <http://code.google.com/p/gridgen-c/>.
- SARIC, W. S. JR, CARILLO, R. B. & REIBERT, M. S. 1998a Leading-edge roughness as a transition control mechanism. *AIAA Paper* 98-0781.
- SARIC, W. S. JR, CARILLO, R. B. & REIBERT, M. S. 1998b Nonlinear stability and transition in 3-D boundary layers. *Meccanica* **33**, 469–487.

- SARIC, W. S., REED, H. L. & WHITE, E. B. 2003 Stability and transition of three-dimensional boundary layers. *Annu. Rev. Fluid Mech.* **35**, 413–440.
- SCHLICHTING, H. 1979 *Boundary-Layer Theory*, seventh edition. McGraw-Hill.
- SCHRADER, L. U., AMIN, S. & BRANDT, L. 2010 Transition to turbulence in the boundary layer over a smooth and rough swept plate exposed to free-stream turbulence. *J. Fluid Mech.* **646**.
- SCHRADER, L. U., BRANDT, L. & HENNINGSON, D. S. 2009 Receptivity mechanisms in three-dimensional boundary layer flows. *J. Fluid Mech.* **618**, 209–241.
- SCHRADER, L.-U., TEMPELMANN, D., BRANDT, L., HANIFI, A. & HENNINGSON, D. S. 2011 Excitation of cross-flow vortices by surface roughness on a swept wing. In *Proceedings of CASI AERO 2011 Conference*.
- SIMEN, M. 1992 Local and non-local stability theory of spatially varying flows. In *Instability, Transition and Turbulence*, pp. 181–195. Springer.
- SOMERS, D. M. & HORSTMANN, K.-H. 1985 Design of a medium-speed, natural laminar-flow aerofoil for commuter aircraft applications. *DLR-IB*. 129-85/26.
- TEMPELMANN, D., HANIFI, A. & HENNINGSON, D. S. 2010 Spatial optimal growth in three-dimensional boundary layers. *J. Fluid Mech.* **646**, 5–37.
- TEMPELMANN, D., HANIFI, A. & HENNINGSON, D. S. 2012 Spatial optimal growth in three-dimensional compressible boundary layers. *J. Fluid Mech.* **704**, 251–279.
- TUFO, H. M. & FISCHER, P. F. 2001 Fast parallel direct solvers for coarse grid problems. *J. Parallel Distrib. Comput.* **61** (2), 151–177.
- WALLIN, S. & JOHANSSON, A. 2000 An explicit algebraic Reynolds stress model for incompressible and compressible turbulent flows. *J. Fluid Mech.* **403**, 89–132.
- WEIDEMAN, J. A. & REDDY, S. C. 2000 A MATLAB differentiation matrix suite. *ACM Trans. Math. Soft.* **26** (4).